Eng. Sci., 2025, **35**, 1582

Engineered Science
DOI: https://dx.doi.org/10.30919/es1582

Modeling of Elastic Oscillations in a Fractured Rock Mass ahead of an Underground Roadway Face

Sh. Aitkazinova,[1,#] Yu. Golovko,[2,#] O. Sdvyzhkova,[2,*] B.Imansakipova,[1,#] D. Babets[2,#] and D. Kirgizbayeva[1,#]

Abstract

The propagation of vibrations in a rock mass arises from sources such as explosions, equipment-induced vibrations, seismic activity, and other dynamic processes. During the interaction of a cutting tool with a coal seam, the rock undergoes compression and deformation, generating stresses in the contact zone. These stresses initiate the propagation of elastic waves within the rock mass. As these waves traverse various geological structures, they undergo reflection and refraction, acting as unique carriers of information about the rock condition. Such waves can serve as indicators of dynamic phenomena, including sudden roadway roof collapses, floor heaving, and rock bursts. This study aims to identify the patterns of vibration propagation generated ahead of the roadway face by the operation of a rock-cutting tool. The research methodology combines analytical modeling of wave processes with numerical analysis of the stress-strain state in the rock near excavations. The study examines the distribution of oscillation amplitudes and displacement velocity as functions of the failure zone length and the ratio of acoustic impedance between the damaged and intact rock mass. These findings contribute to improving the prediction of dynamic phenomena during underground excavations by analyzing acoustic signals.

Keywords: Vibrations; Rock mass; Underground roadway; Failure zone; Numerical simulation.

Received: 19 Jan 2025; Revised: 23 May 2025; Accepted: 29 May 2025.
Article type: Research article.

1. Introduction

The propagation of vibrations within a rock mass is influenced by various sources, including explosions, equipment-induced vibrations, seismic activity, and other factors.[1-3] Each source produces distinct vibration characteristics influenced by its frequency, amplitude, and energy distribution. For instance, when a cutting tool interacts with a coal seam, the rocks experience compression and deformation, generating elastic stresses around the contact zone. These stresses result in the propagation of elastic waves within the rock mass.[4] Elastic waves undergo reflection, refraction, and attenuation as they traverse through heterogeneous structures, making them valuable indicators of the rock mass's condition and precursors to dynamic phenomena such as sudden roof collapses, floor heaving in roadways, rock bursts, and gas emissions.[5-7] These dynamic manifestations pose significant risks to human safety and the integrity of underground infrastructure.[8] Such challenges are prevalent in many mining regions, including the mines of Kazakhstan,[9] where high stress field heterogeneity and complex fracture networks exacerbate these risks. Underground mine accidents in Kazakhstan are mainly associated with rock bursts and gas emissions during underground coal mining. Thus, in 2008, a sudden coal burst and gas emission occurred in a conveyor drift at the Tentekskaya mine (Shakhtinsk, Karaganda region, Kazakhstan), where 5 people died.[10] Similar accidents happened in November 2021 at the Abayskaya mine,[11] and in October 2023 at the Kostenko mine in the city of Karaganda.[12] Dynamic phenomena occur relatively frequently in ore mines. However, in February 2025, a rock burst, accompanied by a collapse of the rock mass and a methane explosion, happened at the Zhomart mine (Ulytau region of Kazakhstan), where copper-sulfide ore is mined.[13]

Undoubtedly, the forecast of such accidents should be improved by various methods, including acoustic. Monitoring wave propagation characteristics is thus critical for developing

---

[1] *Satbayev University (Ministry of Education and Science), st. Satpayeva, 22, Almaty, 050013, Kazakhstan*

[2] *Dnipro University of Technology, av. D.Yavornitskogo,19, Dnipro, 49000, Ukraine*

[#] *These authors contributed to this work equally.*

* *E-mail:* sdvyzhkova.o.o.@nmu.one (O. Sdvyzhkova)

strategies to mitigate dynamic events in underground mines. Therefore, recording the characteristics of the wave propagation as indicators of the rock mass state is extremely important for developing effective strategies for preventing dynamic phenomena in underground mines.[14] The vibration parameters (speed, dispersion, attenuation) are determined by the characteristics of the source (frequency, amplitude, duration of vibrations, location of the source) and the rock acoustic properties (the propagation speed of elastic waves and the attenuation coefficient).[15-17] Numerous scholars have conducted experimental studies to examine the impact of rock qualities and the structural features of the rock mass on the propagation process.[18-23] It has been proven that the wave velocity is typically larger in compact and dense rocks, and the wave velocity decreases with increasing porosity.[24] Zhao *et al*.[25] demonstrate that the seismic wave transmission coefficient increases linearly with growing adhesion between bedding planes. It was proved experimentally that the spectral attenuation coefficient and the average rate of dissipation of harmonic wave energy increase with growing temperature.[26] The impact of fracturing on wave propagation in a rock mass was studied and it has been found that the square of the longitudinal wave velocity is approximately proportional to the modulus of the fracturing direction.[27,28] Zhang *et al*.[29] experimentally studied the dissipation of elastic wave energy in pores and cracks. They discovered that the proportion of high-frequency and low- frequency component of vibration data is sensitive to the degree of rock mass damage.

The impact of fracturing on the propagation of elastic waves in rock formations is examined in the paper.[30] The authors report that in samples of quartz diorite and diabase containing isolated cemented cracks, increasing stress leads to enhanced wave attenuation, along with a reduction in the velocity, amplitude, and dominant frequency of transmitted waves. These effects are primarily attributed to the formation and propagation of microcracks near the joints within the cemented rock.

The systematization and generalization of experimental data on elastic wave propagation in rock masses provided the basis for the subsequent mathematical modeling of these phenomena. In particular, the study of elastic wave behavior ahead of an advancing underground excavation face is of significant interest for predicting and mitigating dynamic events during coal or ore extraction.

It is important to note that mathematical modeling of vibration processes near underground structures involves solving problems related to dynamic elasticity. According to fundamental principles, when an impact load is applied to a body, material points on the impact side immediately move in the direction of the load. These initial displacements transmit momentum to adjacent particles, resulting in a stress wave propagating through the material. By applying Newton's second law, the continuity condition, and the balance of forces across the interaction surfaces, the classical wave equation can be derived, providing a fundamental model for elastic wave propagation. A one-dimensional model is employed to investigate free vibration phenomena in steel samples of complex geometries.[31] Similarly, Xu and Lognonné apply a one-dimensional elastic medium framework to model ground surface deformations under atmospheric pressure fluctuations. Their approach, based on eigenfunction theory, allows for the simulation of mechanical deformation as plane waves propagating through a homogeneous medium.[32]

Andrukhiv *et al*.[33] introduce a mathematical model describing longitudinal oscillations in a homogeneous body of constant cross-section subjected to impulsive loads. The governing equation is a hyperbolic partial differential equation featuring a small parameter within the discrete right-hand side. This formulation enables the derivation of first-order approximations for the key parameters governing elastic body oscillations. The findings demonstrate that even in unperturbed motion, the system's natural frequency is amplitude-dependent, implying the possibility of both resonant and non-resonant responses under periodic impulse loading. These responses are determined by the material's physical and mechanical properties and the oscillation amplitude.

Mechanical wave propagation in an isotropic elastic solid is modeled using the classical Navier equation expressed in vector form, extending the formulation to three-dimensional space. The model incorporates a Kelvin–Voigt Fractional Derivative (KVFD) wave equation, which is numerically solved using a Finite Difference Time Domain (FDTD) scheme. This approach serves as the foundation for the development of novel elastography techniques.[34]

The reviewed studies collectively demonstrate the inherent complexity of mathematically describing wave propagation, even within homogeneous isotropic continua. This complexity increases substantially when modeling fractured rock masses.[35] Zhang *et al*.[36] apply elastodynamic principles to investigate wave propagation in rock masses containing structural discontinuities. The Zoeppritz equations are employed to describe wavefield decomposition, leading to the development of a seismic wave response model. The results indicate that stress waves interacting with discontinuity interfaces may convert into tensile waves, inducing tensile stresses via wave scattering. This process facilitates energy dissipation and accelerates the development and propagation of internal defects within the rock mass. Recognizing the intricacy of the full mathematical formulation, the authors propose a simplified model utilizing elastic wave velocity and elastic modulus, thereby enhancing the model's applicability to engineering practice.

Given the challenges associated with obtaining analytical solutions within the framework of dynamic elasticity theory, the use of idealized assumptions and numerical methods is a reasonable and widely adopted approach when modeling wave propagation in fractured rock masses.[37,38]

This study aims to analyze the mechanisms underlying elastic wave propagation induced by the interaction between rock-cutting tools and the rock mass. By examining vibration characteristics ahead of an underground excavation face, this research seeks to enhance predictive capabilities for dynamic phenomena during roadway development, thereby contributing to safer and more efficient excavation processes.

2. Analytical prerequisites for analyzing the propagation of vibrations in a rock mass

2.1 Propagation of elastic waves

Roadway excavation induces stress redistribution within the surrounding rock mass, resulting in the formation of a failure or plastic zone. This zone, characterized by intense fracturing, represents the transition of rock material from an elastic state to a structurally altered condition.[39,40] The extent and properties of the failure zone depend on various geomechanical factors.[41,42] Within this zone, the mechanical and acoustic properties of the rock differ significantly from those of the intact rock mass.[43] Consequently, the altered acoustic characteristics within the failure zone provide critical insights into the structural integrity of the surrounding rock mass and the dynamics of stress redistribution.

With a certain degree of idealization, a portion of the rock mass in front of the roadway face can be considered a semi-infinite rod (infinite in one direction only) consisting of two non-separable sections with different acoustic characteristics. Let a semi-infinite elastic rod with Young's modulus $E_0$and density ρ_0 have a beginning section of finite length l, which is characterized by distinct elastic modulus $E_1$and density ρ_1. Oscillations in the rod are caused by a longitudinal harmonic force acting on the rod end constantly with a circular frequency $\omega$and amplitude σ_0. In terms of geomechanics the beginning section of the rod imitates the zone of failed rocks ahead of the roadway face. The goal of this idealization is to ascertain how the failure zone size and acoustic characteristics within this zone affect the parameters of the elastic wave propagation in the rock mass.

Let the origin of coordinates be placed on the boundary of the finite and infinite sections of the rod, *i.e.*, on the interface of homogeneity. Further, the quantities with index *1* are related to the beginning (finite) section, and quantities with index *0* are related to the remaining infinite part of the rod.

The following variables are involved to model the propagation of oscillations: coordinate x, time t, displacement u_k, speed of sound c_k, density ρ_k, *k*=0,1. Some relative variable should be involved to simplify the mathematical model. Let l be a scale for the length, $\frac{l}{c_0}$ be a scale for time, c_0 be a scale for the sound speed, σ_0 be a scale for the stress, $\frac{\sigma_0 l}{c_0^2\rho_0}$ be a scale for the displacement, $\frac{\sigma_0}{c_0\rho_0}$ be a scale for the velocity of the displacement, $\frac{c_0}{l}$ be a scale for the circle frequency. Then the basic system of equations in dimensionless quantities looks like Eqs. (1)-(4):

$$\frac{\partial^2 u_k}{\partial_{t^2}} = c_k^2\frac{\partial^2 u_k}{\partial_{x^2}}, k = 0,1 \tag{1}$$

$$u_1(t,0) = u_0(t,0) \tag{2}$$

$$c_1^2\rho_1\frac{\partial u_1}{\partial x}(t,0) = \frac{\partial u_0}{\partial x}(t,0) \tag{3}$$

$$c_1^2\rho_1\frac{\partial u_1}{\partial x}(t,-1) = sin(\omega t) \tag{4}$$

In dimensionless quantities we have $c_0 = 1$, and $c_1\rho_1$ can be considered a ratio of the acoustic resistances (rigidities) of the beginning section and the rest of the semi-infinite rod. The parameters of the given problem are the quantities $c_1,\ \rho_1$и ω. The solution of the system of Eqs. (1) – (4) can be found in the form Eq. (5) satisfied Eq. (1):

$$u_k(x,t) = A_k\, exp[\, i(\frac{\omega x}{c_k} - \omega t)] + B_k\, exp[\, -i(\frac{\omega x}{c_k} + \omega t)] \tag{5}$$

where A_k, B_k are the complex amplitudes of waves propagating to the right and left sides of the rod with respect index k and i is imaginary unit ($i^2 = -1$).

Since in the semi-infinite rod (at $x > 0$) the disturbances are not reflected and can only propagate to the right (radiation conditions), we put $B_0 = 0$. From now on we omit the time-dependent term $exp(-i\omega t)$.

Substituting Eq. (5) into Eqs. (2)-(4), one can obtain the system of equations:

$$A_1c_1\rho_1\omega\, exp(-i\frac{\omega}{c_1}) - B_1c_1\rho_1\omega\, exp(i\frac{\omega}{c_1}) = 1 \tag{6}$$

$$A_1 + B_1 = A_0 \tag{7}$$

$$A_1 - B_1 = \frac{1}{c_1\rho_1}A_0 \tag{8}$$

The values of complex amplitudes A_0, A_1, B_1 derived from Eqs. (6)-(8) should be substituted in Eq. (5) to obtain the following expression for displacements:

$$\mu_1 = \frac{\Delta}{\omega c_1 \rho_1}\{c_1\rho_1[\mathrm{acos}\,(\frac{\omega x}{c_1}) - \mathrm{bsin}\left(\frac{\omega x}{c_1}\right)] + \mathrm{i}[\mathrm{asin}\left(\frac{\omega x}{c_1}\right) + c_1^2\rho_1^2 b cos(\frac{\omega x}{c_1})]\} \tag{9}$$

$$u_0 = \frac{\Delta}{\omega}\{[a\,cos(\omega x) - \rho_1 c_1 b\,sin(\omega x)] + i[a\,sin(\omega x) + \rho_1 c_1 b\,cos(\omega x)]\} \tag{10}$$

where $a = cos\left(\frac{\omega}{c_1}\right)$, $b = sin\left(\frac{\omega}{c_1}\right)$, $\Delta = [c_1^2\rho_1^2 b^2 + a^2]^{-1}$.

Given expressions generalizes the solution for the finite section of the rod ($c_1 \to 0$ and $c_1 \to \infty$) and infinite part ($c_1 = 1$), which can be found from Eqs. (9) and (10) as special cases.

Solution given by Eqs. (9) and (10) allows analyzing the features of wave processes dependently on the length of the beginning (finite) section of the rod associated with failure zone in front of the roadway face as well as with the difference in acoustic properties in beginning finite section and remaining infinite part of the rod. Further, based on the obtained solutions, we assume that $c_1 < 1$, $\rho_1 \leq 1$.

Eq. (9) indicates that resonances in the commonly understood sense, where the amplitude rises infinitely under loading at a specific frequency, are only feasible in the idealized conditions ($c_1 \to 0$, $c_1 \to \infty$), that is, strictly speaking, for finite rods. Simultaneously, oscillations with an amplitude exceeding the amplitude of the load are observed for specific ratios c_1, ρ_1 and ω at certain points along the rod beginning section. Fig. 1 illustrates the displacements at different time and points of the rod as an example. The greatest displacement at the point with coordinate $x = -0{,}5$ is much greater than the displacement at the loaded end of the rod ($x = -1$).

Based on Eqs. (9) and (10) the real amplitudes of oscillation can be derived for infinite part of the rod in Eq. (11):

$$U(\omega, c_1, \rho_1) = \frac{1}{\omega\sqrt{\rho_1^2 c_1^2\,sin^2\left(\frac{\omega}{c_1}\right) + cos^2\left(\frac{\omega}{c_1}\right)}} \tag{11}$$

and for beginning (finite) section:

$$U(x, \omega, c_1, \rho_1) = \frac{1}{\rho_1 c_1 \omega}\sqrt{\frac{\rho_1^2 c_1^2\,cos^2\left(\frac{\omega x}{c_1}\right) + sin^2\left(\frac{\omega x}{c_1}\right)}{\rho_1^2 c_1^2\,sin^2\left(\frac{\omega}{c_1}\right) + cos^2\left(\frac{\omega}{c_1}\right)}} \tag{12}$$

The amplitude of displacements given by Eq. (9) in the infinite part of the rod does not depend on the coordinate x. But inside the beginning (finite) section, the amplitude given by Eq. (10) alters with a change in the point position and can significantly exceed the amplitudes that occur at the loaded end of the rod ($x = -1$).

Studying the extrema of the function Eq. (12) shows that the amplitudes of displacements reach maximum values at the points with coordinates:

$$x_k = -\frac{\pi c_1(2k-1)}{2\omega};\ k = \overline{1, K};\ K = \left\lfloor\frac{\omega}{\pi c_1} + \frac{1}{2}\right\rfloor;\ \omega > \frac{c_1\pi}{2} \tag{13}$$

Maximum values of the amplitudes are equal:

$$U_{max}(\omega\rho_1 c_1) = U(x_1\omega\rho_1 c_1) = \frac{1}{\omega\rho_1 c_1\sqrt{\rho_1^2 c_1^2\,sin^2\left(\frac{\omega}{c_1}\right) + cos^2\left(\frac{\omega}{c_1}\right)}}_{max} \tag{14}$$

Note that K equals to the number of points within the rod beginning section in which the maximum displacement amplitudes are achieved, x_K is the coordinate of the amplitude maximum closest to the load point, and x_1 is the coordinate of the amplitude maximum closest to the infinite part of the rod. The amplitude of displacement at the point of load application has the form:

$$U_{-1}(\omega, c_1, \rho_1) = U(-1, \omega, c_1, \rho_1) = \frac{1}{\rho_1 c_1 \omega}\sqrt{\frac{\rho_1^2 c_1^2\,cos^2\left(\frac{\omega}{c_1}\right) + sin^2\left(\frac{\omega}{c_1}\right)}{\rho_1^2 c_1^2\,sin^2\left(\frac{\omega}{c_1}\right) + cos^2\left(\frac{\omega}{c_1}\right)}} \tag{15}$$

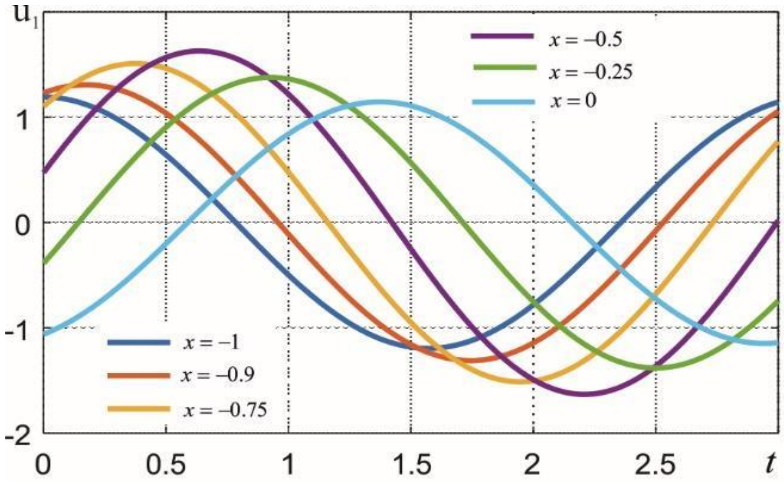

Fig. 1: Displacements at different points x of the beginning (finite) section depending on time at the values $c_1 = 0{,}7$; $\rho_1 = 1$.

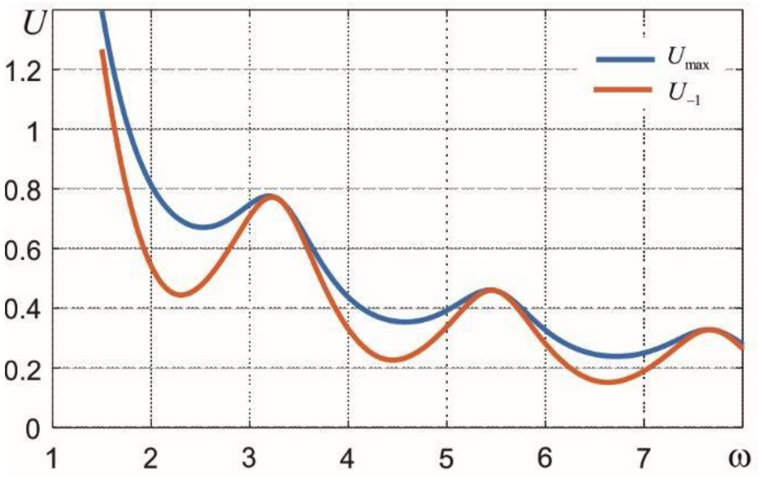

Fig. 2: Maximum amplitude (U_{max}) of displacements at internal points of the rod beginning section and the amplitude of displacement at the point of load application (U_{-1}) at $c_1 = 0{,}7;\quad \rho_1 = 0.9$.

The graphs of relationships given by Eqs. (14) and (15) (Fig. 2) demonstrate that function represented by Eq. (15) attains identical maximum values at the same frequencies as function given by Eq. (14). Thus, we can write that: $U_{\max}(\omega_{\max}, c_1, \rho_1) = U_{-1}(\omega_{\max}, c_1, \rho_1)$.

The amplitude magnitudes should be related to the value occurring at the point of load application for a more realistic analysis of the oscillation distribution along the beginning section of the rod, that is, we will further analyze the quantities:

$$\overline{U}(x,\omega,c_1,\rho_1) = \frac{U(x,\omega,c_1,\rho_1)}{U_{-1}(\omega,c_1,\rho_1)} = \sqrt{\frac{\rho_1^2 c_1^2 \cos^2\left(\frac{\omega x}{c_1}\right) + \sin^2\left(\frac{\omega x}{c_1}\right)}{\rho_1^2 c_1^2 \cos^2\left(\frac{\omega}{c_1}\right) + \sin^2\left(\frac{\omega}{c_1}\right)}} \quad (16)$$

The amplitudes of oscillations along the beginning section, determined by Eqs.(15) and (16), are obtained as functions of the position coordinate χ, normalized by the length of the initial section l. Thus, the actual amplitudes of oscillations are directly governed by this parameter.

As noted above, within the framework of the adopted model and by analogy with geomechanically processes in rock masses, the beginning section of the semi-infinite rod is associated with a horizontally extending region in the rock ahead of the excavation face, where the rocks failed. Determining the extent of this failure zone constitutes a separate problem in rock mechanics, which is addressed in the following section.

2.2 Size of the failure zone ahead of the roadway face

The elastic-plastic solution concerning the stress-strain state (SSS) around a long horizontal excavation is employed to delineate the area of failed rocks. While the waveguide is idealized as a semi-infinite rod for theoretical considerations, this study incorporates a realistic 3D model of an arch-shaped underground excavation (roadway) to accurately calculate the dimensions of the failure zone. The length of this zone l, extending in front of the excavation face is of greatest concern since it is responsible for the support design and that is the parameter l involved in mathematical model of the wave propagation.

The finite element method (FEM), a robust and well-validated computational approach,[16,44] is utilized via the RS3 Rocscience software to construct a detailed 3D model of the roadway (Fig. 3). The delineation of the failure zone around the excavation is based on the generalized Hoek-Brown criterion,[38] which accounts for the rock mass's structural and material properties.

The Geological Strength Index (GSI), introduced by Hoek and Brown,[45] serves as a comprehensive measure of rock mass quality, effectively integrating heterogeneity and structural irregularities into the analysis. The relationship between the strength and deformability parameters of the rock mass and GSI is defined by Eq. (17), incorporating the disturbance factor D to account for blast-induced damage:

$$E_m(GPa) = \left(1 - \frac{D}{2}\right)\sqrt{\frac{\sigma_{CI}}{100}} * 10^{(GSi-10)/40} \quad (17)$$

In the case of intact rock, $D=0$, indicating no disturbance. However, near the excavation face, disturbances induced by blasting and rock cutting result in $D>0$. For instance, as specified in Table 1,[38] D is assigned a value of 0.5 when disturbance manifests as floor heaving. Consequently, the ratio of the deformation moduli between the finite segment of the rod (failure zone ahead of the roadway face) and infinite part of the rod (the surrounding intact rock mass) is determined by Eq. (18):

$$\frac{E_1}{E_0} = 1 - \frac{D}{2} = 0.75 \quad (18)$$

This ratio will subsequently be employed in the wave propagation model to characterize the acoustic properties of the failure zone relative to the undisturbed rock mass.

2.3 Object of study

As it was mentioned above, the propagation of elastic waves in the rock mass can initiate dynamic phenomena such as bumps, collapses, and rock bursts. Understanding the hazards of sudden collapses prompted studies specific to the Akzhal

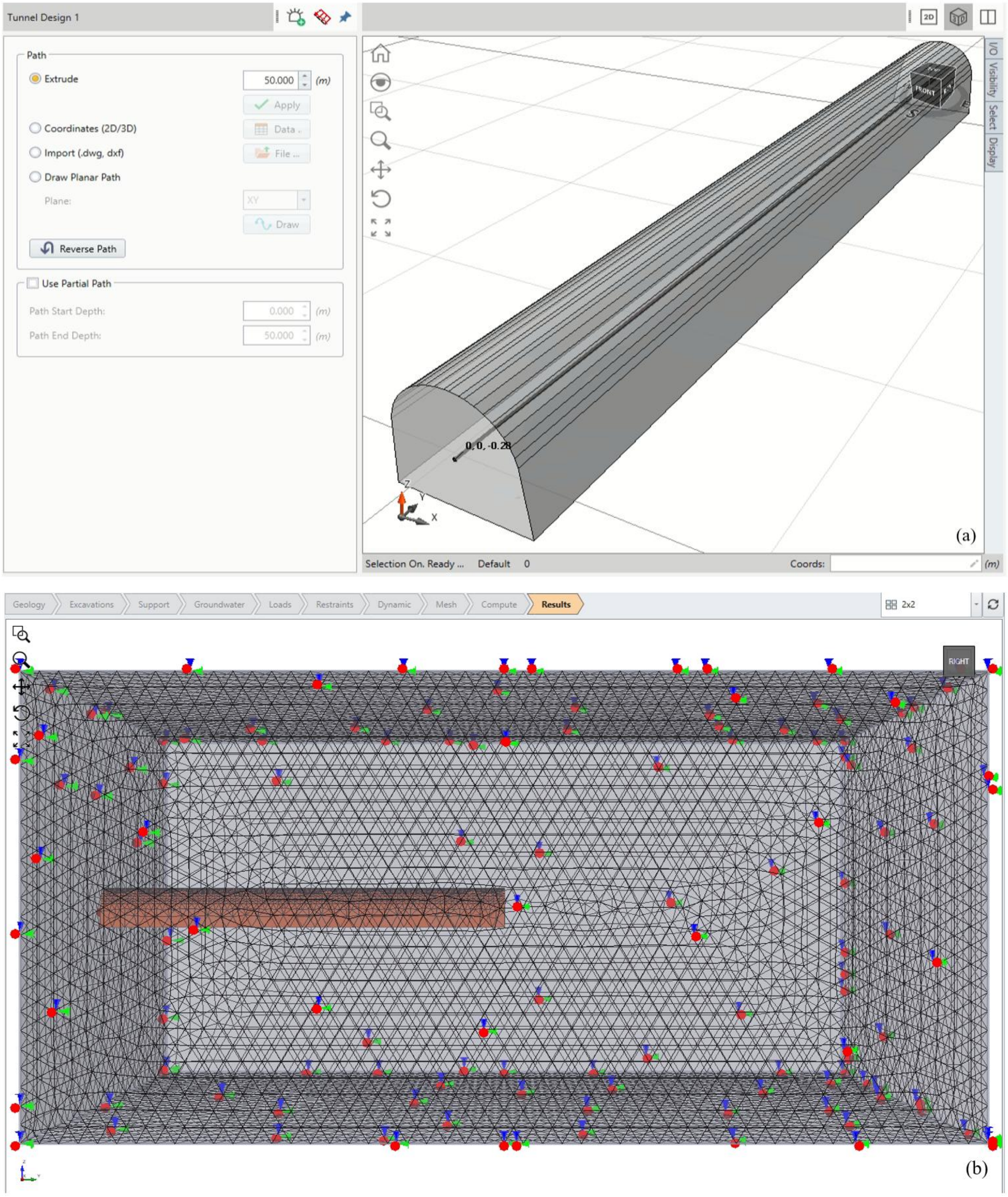

Tunnel Design 1

Path

● Extrude 50.000 (m)

○ Coordinates (2D/3D)

○ Import (.dwg, dxf)

○ Draw Planar Path

Plane: XY

☐ Use Partial Path

Path Start Depth: 0.000 (m)

Path End Depth: 50.000 (m)

Selection On. Ready ... Default 0

Fig. 3: (a) Design scheme; (b) finite element mesh for calculating the stress-strain state of the rock mass and the failure zone ahead of the face.

lead-zinc ore deposit located in Karaganda region of Kazakhstan. The deposit is situated within the sublatitudinal syncline of the Akzhal-Aksoran zone. The host rock sequence primarily consists of sandy limestone and calcareous sandstone. On the western flank of the deposit, these sedimentary formations are intruded by stock-like bodies of diorite-porphyrites, which have induced a broad metasomatic alteration halo within the surrounding limestones (Fig. 4).

Approximately 85% of the ore reserves are hosted within massive limestone units, with the remaining 15% distributed among other lithological types. The ore zone exhibits a complex internal structure, comprising sheet-like and saddle-shaped ore bodies, as well as vein-disseminated mineralization. These ore bodies display significant variability in both strike and dip, characterized by constrictions, swellings, bifurcations, and re-merging structures. The strike lengths of individual ore bodies range from 20 to 1000 meters, with dip extents varying between 10 and 350 meters. The thickness of the ore bodies spans from 2 to 70 meters. The deposit contains lead-zinc and zinc-dominant ores, primarily composed of sphalerite, galena, pyrite, and chalcopyrite. Accessory minerals include cadmium, silver, gold, thallium, germanium, indium, tellurium, and selenium. The ore textures vary from disseminated and vein-disseminated to massive forms. The average metal contents within the ore amount to 1.14% Pb, 4.87% Zn, and 0.14 g/t Au.

From a genetic perspective, the deposit is associated with skarn metasomatic processes, which developed as a result of interactions between magmatic intrusions and carbonate host rocks. These processes led to the formation of skarns enriched in lead- and zinc-bearing sulfide minerals. Hydrothermal fluids of magmatic origin contributed further to mineralization by introducing sulfide phases such as sphalerite (ZnS), galena (PbS), and pyrite (FeS_2) into the skarn-altered rocks. The presence of elements commonly associated with hydrothermal systems, including silver, indium, and cadmium, further supports the hydrothermal contribution to ore formation. Consequently, the Akzhal deposit is classified as a skarn-hydrothermal type.

The initial development of the Akzhal deposit was conducted via open-pit mining; however, subsequent operations transitioned to underground mining methods. The underground workings are primarily located within massive siliceous-clayey limestones with an average thickness of up to 20 meters. The geological structure of the Akzhal deposit is characterized by the presence of disjunctive faults of varying amplitudes, accompanied by zones of rock fracturing and schistosity. These structural discontinuities result in significant heterogeneity in the strength and deformation properties of the rock mass across different sections of the mine. To evaluate these mechanical characteristics, rock samples were obtained by core drilling from boreholes located in areas where horizontal roadways were excavated and where varying degrees of rock fracturing were observed. Drilling of wells with a diameter of BQ (60 mm) was carried out by a mobile rig Diamec232 (Atlas Copco).

The rock samples were tested in Satbayev University Geomechanics Laboratory in accordance with ASTM D7012-14 Standard. The UCT-1000 servohydraulic system from GCTS was employed to determine uniaxial compressive strength and Young's modulus.

The histograms in Fig. 5 demonstrate the statistical distributions of the limestone compressive strength built for samples taken from four sites where the different rock mass quality was observed. Each site's sample strength varies by 30–35% and the same statistical variation (30-40%) has been discovered for Young's modulus.

In accordance with mechanical properties and the fracturing parameters including the quality of joints surfaces, the GSI values have been assigned for each explored site of the mine field using the methodology.[45]

Site # 1 description. The site is situated in the air roadway of the level of 355m.The in situ observations demonstrate rock mass jointing in the roof and walls of the excavation, but no obvious rock deformations evident are not seen. The mean uniaxial compressive strength of limestone is 79 MPa according sampling at this site (Fig. 5a), the modulus of elasticity is 8100 MPa, and the Poisson ratio is 0.2. The core samples taken from drilled holes demonstrate that the index RQD (Rock Quality Determination) ranges from 75% to 90%. The distance between joints varies in the range from 60 to 200 mm. The joint walls observed on the rock outcrops are slightly weathered and rough. The length of the joints reaches up to 2 m, the degree of the joint opening varies from 1mm to 5 mm, and the joint space is filled with a hard filler. Most of the joints observed in the mine are steeply dipping with inclination angles of α=70°-80°. Based on this information, according the method recommended in [36], the index RMR (Rock Mass Rating) should be calculated first. Then relationship $GSI = RMR-5$ can be applied. In case of site #1 $RMR=54$, and $GSI = 49$.

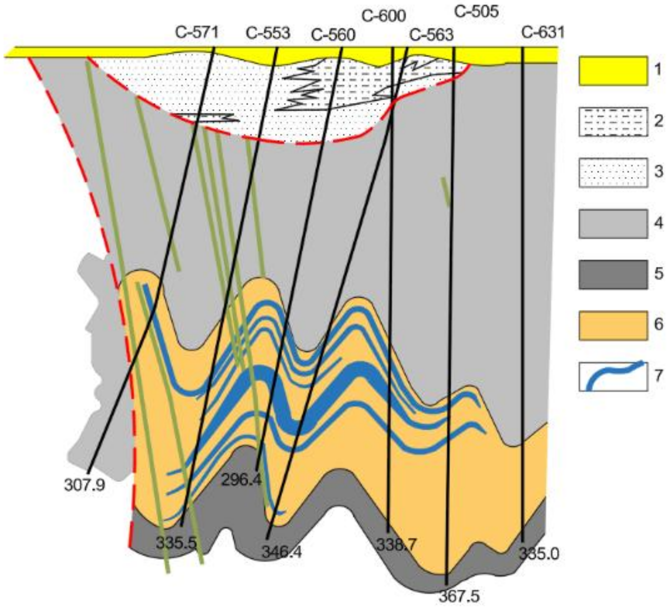

Fig. 4: Geological section of the central part of the Akzhal deposit: 1 - clays; 2 - quartz porphyry; 3 - sandstone; 4 - gabbro-diabases, diorite porphyrites; 5 - siliceous-clayey limestones (supra-ore strata); 6 - massive limestones (ore-bearing strata); 7 - hydrothermal-sedimentary ores with zinc content of 0.5-2.5%; 8 - hydrothermal-metasomatic ores with zinc content of 1.0-3.0%.

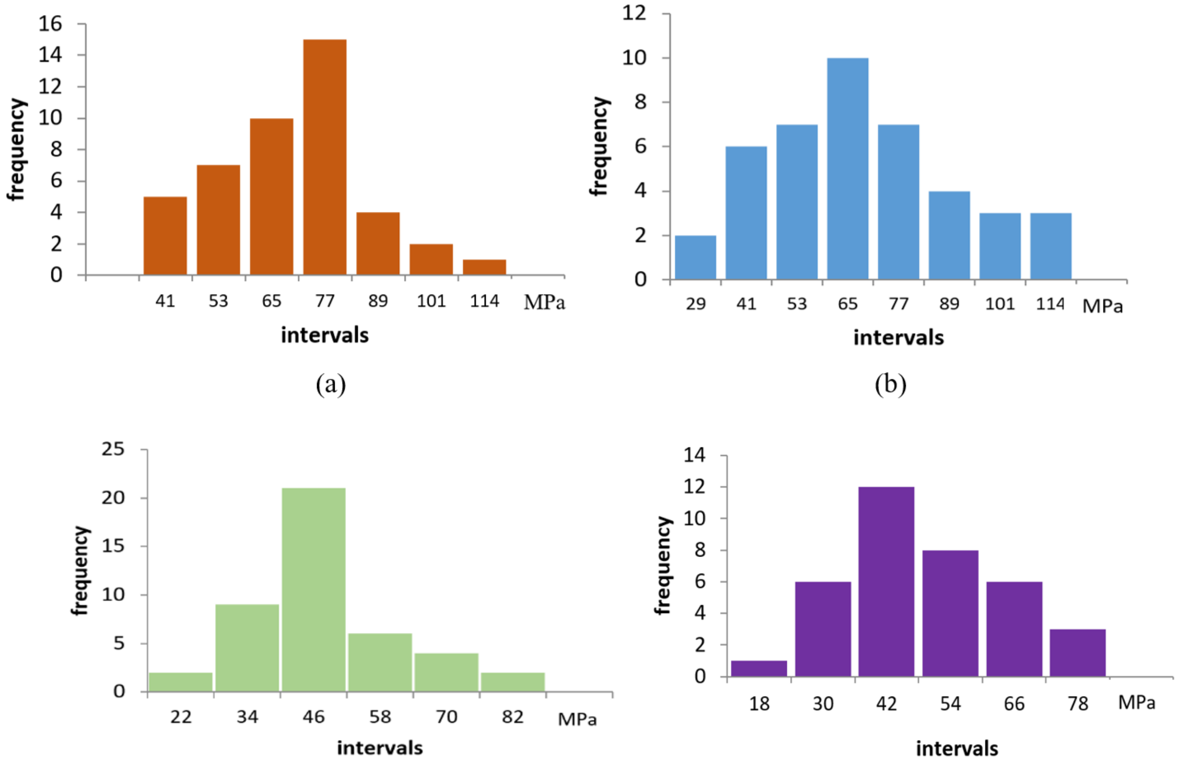

(a) (b)

(c) (d)

Fig. 5: Histograms of frequencies related to limestone compressive strength: (a) site #1; (b) site #2; (c) site#3; (d) site #4.

Site # 2 description. The site is located in the transport roadway of the level of 355m. The fracturing parameters are similar to those obtained for the site #1, but the joints at this site have smooth walls and are filled with soft material. Visual monitoring revealed rock delamination in the roof and walls of the excavation. Laboratory testing of samples collected from this site showed some reduction in compressive strength of limestone up to 67 MPa (Fig. 5b) and reduction in elasticity modulus up to 7650 MPa. The value of Poisson ratio is 0.28. The studies of drilled cores displayed the variation of RQD index in the range from 60% to70%. The decrease in RQD and deterioration in the quality of the joint surface reduces the RMR index to 46, and the GSI index to 41, respectively.

Site # 3 description. This section of the transport roadway of 355m level is located close to a geological fault with an amplitude of 10 m, which predetermined deterioration in rock mass quality in this area. Surveys revealed numerous rock delamination and support failure (metal mesh breakthrough) in the roof and walls of the excavation. The mean uniaxial compressive strength of limestone (Fig. 5c) decreases to 48 MPa in this site according the sample testing. Young's modulus decreases as well to the value of 3500 MPa, and Poisson's ratio is determined as 0.3. The RQD index calculated according to the structure of the drilled core falls to 35%. The fracturing parameters are similar to those observed for the site #2, but the smooth surfaces of the joints are waterlogged, since the water inflow is greater in this area. Not only the joint walls are wet, but the entire outcrop surface is moist as well. The GSI index falls to 30 as a result of the RMR index declining to 35.

Site # 4 description. The site is also the section of the 355m-level transport roadway, but it is situated closest to the fault in the intense fracturing area. Multiple delaminations, rock falls, metal mesh breakage and rock bolt failures are observed here. The mean uniaxial compression strength of limestone according sampling at this site (Fig. 5d) drops to the value of 36 MPa and Young's modulus decreases to 2800 MPa, and Poisson's ratio is 0.32. Drilling of wells ahead of the roadway face discovered the significant rock fragmentation described by RQD=30-35%. Water drips are observed both from the wells and in the roadway roof. In this regard, the index RMR should be lowered as much as to 27, and respectively the GSI index should be reduced to the value of 22.

The ratings RMR and GSI determined for the four study sites were utilized in conjunction with the strength and deformability parameters of the rock mass to perform a FEM-analysis of the stress-strain state (SSS) in the vicinity of the roadway. Incorporating these ratings enhances the fidelity of the numerical model by accounting for varying degrees of rock fracturing, thereby aligning the simulations more closely with field conditions. This approach enables a more accurate identification of the failure zone ahead of the roadway face and facilitates the determination of the length of the zone characterized by altered acoustic properties, which differ from those of the undisturbed rock mass.

3. Results and discussion

3.1 Determining the failure zone ahead of the roadway

Site#1. The simulation of the stress-strain state (SSS) of the rock mass at the site was conducted using a Geological Strength Index (GSI) value of 49. Based on this value, the parameters of the generalized Hoek-Brown failure criterion were determined utilizing the RSDATA Rocscience software. The resulting distribution of maximum principal stresses and total displacements aligns with the typical elastic-plastic behavior observed in cases of single horizontal excavations. The stress peak in surrounding rocks reaches $2.2_{\gamma}H$, where $_{\gamma}$ represents the rock unit weight and H denotes the roadway depth. This peak stress occurs 2.1 meters away from the excavation face, within the undisturbed rock mass, where rock failure also initiates at this distance ahead of the face. The failure zone extends 2.1 meters ahead of the roadway face under the specific conditions of the site #1. This failure zone is considered a region of the rock mass with altered acoustic properties, and the derived value l=2.1 is subsequently employed in the wave propagation modeling.

Site#2. Deterioration of the rock mass quality is observed in this area, which is indicated by the decrease in GSI to the value of 41. The concentration of maximum principal stresses ahead of the roadway face decreases from the value of 2.2_{γ}H calculated for the site# 1 to the value of 2.0 $_{\gamma}$H. The stress peak shifts into the massif by 3.9 meters, which outlines the dimension of failure zone under the specific conditions of site#2. Thus, the failure zone extends 3.9 meters ahead of the roadway face under the specific conditions of site #2. The calculated value l= 3.9 is then used in wave propagation modeling, and this failure zone is regarded as a section of the rock mass with changed acoustic characteristics.

Site#3. This area is distinguished by the close vicinity of a geological fault, which causes the more extensive fracture and rock wetness, as seen by a low geological index value (GSI=30). The stress concentration ahead of the excavation face decreases in comparing with sites#1 and site#2 and reaches 1.9_{γ}H. The failure zone ahead of roadway face is up to 6.0 meters long at the site#3 that corresponds to the decline in the rock mass quality as defined by GSI=30. Therefore, under the particular conditions of site #3, the failure zone extends 6.0 meters ahead of the roadway face. The wave propagation modeling is then performed using the computed value of l=6.0, and this failure zone is thought of as a portion of the rock mass with altered acoustic properties

Site #4. This site is situated near a geological fault, similar to site #3. The location caused the specific features of stress distribution and displacements values due to the weakest rock mass and the highest intensity of jointing. Additionally, significant water content is observed in the excavation roof, further compromising the stability of the rock mass. These factors are reflected in the low Geological Strength Index (GSI = 22). Under such conditions, as anticipated, the stress concentration ahead of the excavation face is minimal and reaches only 1.7_{γ}H, while displacements are maximum and failure the zone is the largest, extending to 8.2 meters. Thus, as the quality of the rock mass deteriorates, the peak stress ahead of the excavation face shifts deeper into the intact massif, leading to an expansion of the failure zone. This enlargement of the failure zone correlates with an increase in the area exhibiting altered acoustic properties. Fig. 6 illustrates the relationship between the length of the zone with altered acoustic properties and the GSI value.

Approximation of the simulation results by an exponential function $l=24,5exp(-0,05GSI)$ with determination index $R^2=0,9674$ reveals that with further development of fracturing and water content, and consequently with a decrease in the GSI index, the length of the failure zone in front of the roadway face can rise to 10 m.

Within the framework of the vibration propagation model proposed above, the determined length of failure area l ahead of the excavation face corresponds to the length of the beginning (finite) section of the rod that simulates the propagation path.

Knowing the actual length of the failure zone ahead of the roadway face, we can obtain the corresponding amplitude-

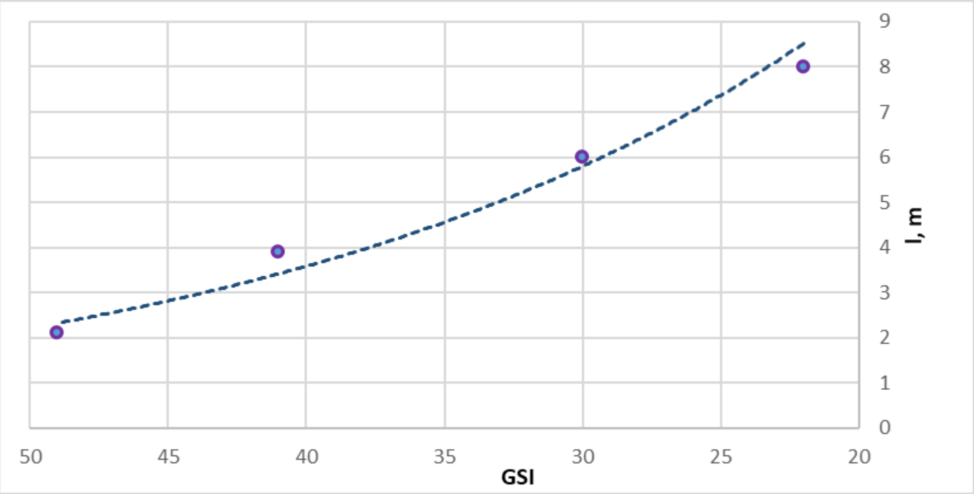

Fig. 6: Increase in the length l of the failure zone ahead of the excavation face with a decrease in the geological index GSI.

frequency spectrum of oscillations that arise in the rock mass during the operation of the rock-cutting tools. Next, we continue to consider the harmonic loading of the rock mass by analogy with the loading of a semi-infinite rod under a harmonic force.

3.2 Amplitude-frequency analysis of oscillations produced by harmonic loading of rock mass.

The measurement of kinematic characteristics is usually performed utilizing velocimeters or accelerometers, i.e. the recorded signals are proportional to the velocity or acceleration at the point of contact of the sensor with the solid at the installation point.

Under the above considered harmonic loading of the semi-infinite rod, the displacement velocity at the point of load application looks like Eq. (19):

$$v_1|_{x=-1} = -i\omega u_1|_{x=-1} = \frac{-i\Delta}{c_1\rho_1}\{c_1\rho_1\left[a\cos\left(\frac{\omega}{c_1}\right) + b\sin\left(\frac{\omega}{c_1}\right)\right] + i\left[-a\sin(\frac{\omega}{c_1}) + c_1^2\rho_1^2 b\cos\left(\frac{\omega}{c_1}\right)\right]]\} \quad (19)$$

And the amplitude of the velocity at the same point is given by Eq. (20):

$$V_{-1}(\omega, c_1, \rho_1) = \frac{1}{\rho_1 c_1}\sqrt{\frac{\rho_1^2 c_1^2\cos^2\left(\frac{\omega}{c_1}\right)+\sin^2\left(\frac{\omega}{c_1}\right)}{\rho_1^2 c_1^2\sin^2\left(\frac{\omega}{c_1}\right)+\cos^2\left(\frac{\omega}{c_1}\right)}} \quad (20)$$

The maximum values of the velocity amplitude equal to $\frac{1}{\rho_1^2 c_1^2}$ are reached at the frequency value:

$$\omega = \frac{\pi c_1}{2}(2k-1), k = 1,2,\ldots \quad (21)$$

Dependences given by Eqs. (15)-(20) can be considered as the frequency response of the system, when the input signal is the loading force, and the output signal is the displacement velocity at the point of load application. At $\omega > \frac{c_1\pi}{2}$ the same dependencies describe the frequency response with an output signal in the form of the maximum velocity amplitude and the maximum displacement at the internal points of the rod beginning section, *i.e.*, in the range of (-1, 0).

The frequency values at which the amplitude reaches the maximum are of greatest interest. When considering displacement amplitudes, finding the frequencies that maximize these amplitudes involves solving a transcendental equation. However, the frequencies determined this way differ negligibly from those found by Eq. (21), starting from *k=2* (Fig. 7).

Thus, if the force load has a uniform and sufficiently broad spectrum, the components at the frequencies given by Eq. (16) will stand out in the spectrum of displacement velocity. The load spectrum is limited and typically decreases as the frequency increases. Therefore, the lower frequencies from the set of values:

$$\omega_1 = \frac{\pi c_1}{2}, \omega_2 = \frac{3\pi c_1}{2} \quad (22)$$

where ω_1 and ω_2 are the most informative.

At $\omega = \omega_1$ the maximum amplitude of oscillations in the rod beginning section is observed only at the point of load application (*K=1*). However, there is no extremum in the frequency response for displacements at this point. Components with frequency $\omega = \omega_1$ will be amplified in the displacement velocity spectrum, but this does not indicate the presence of oscillations with the same displacement amplitude at internal points of the rod beginning section. The observed increase in these components can only be used to estimate the length *l* of the rod beginning section.

At $\omega = \omega_2$ oscillations with maximum displacement amplitude also occur at a point within the internal part of the rod beginning section and this can be considered a more dangerous situation in terms of the potential dynamic event.

To analyze the effect of the beginning section length on the spectrum of the recorded signal, let us pass in Eq. (22) to dimensional frequencies (ω_1^*, ω_2^*)and the dimensional sound velocity (c_1^*) in the beginning section:

$$\omega_1^* = \frac{\pi c_1^*}{2l^*}, \omega_2^* = \frac{3\pi c_1^*}{2l^*} \quad (23)$$

To avoid ambiguity, all dimensional quantities are marked with an asterisk (*) hereafter. We assume that a signal proportional to the velocity at the point of the load application is available. For example, the initial signal could come from a velocimeter installed on a rock-cutting tool or from a velocimeter located close to the point where the tool impacts the rock mass.

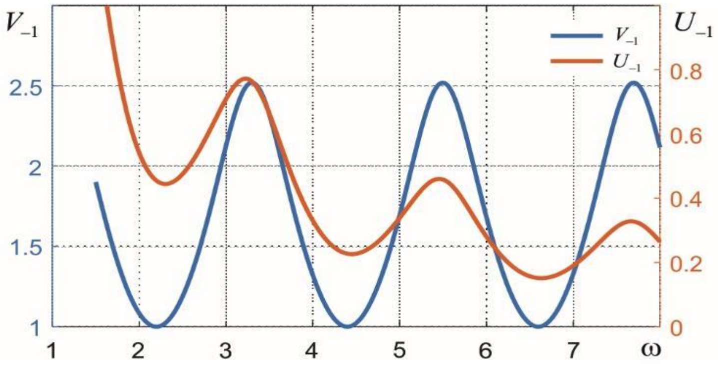

Fig. 7: Amplitude-frequency characteristics for displacement and displacement velocity at the point of load application when $c_1 =$ 0,7; $\rho_1 = 0.9$.

Let the spectrum of the load remain unchanged while the length of the rod beginning section continuously decreases. Then, as follows from the given expressions, the components with increasing frequencies will be amplified in the recorded signal spectrum. For predicting dangerous situations, it is crucial to monitor the growth of components at the level of ω_2^*. To perform such forecast based on the recorded signal spectrum, it is necessary to know the parameters of the zones with altered properties. In section 3.1, the length l of such zones has been determined using FEM-analysis within the Hoek-Brown strength theory (Table 1). Thus, in a first approximation, we involve the length $(l^*)$of the rod beginning section for modeling the vibration propagation ahead of the excavation face. Note, that instead of circular frequencies (ω^*), the cyclic frequencies $\left(f^* = \frac{\omega^*}{2\pi}\right)$ usually used in measurements are indicated in Table 1 and the frequency values are rounded to whole values.

Amplitude of oscillations within the beginning section of the rod with altered elastic characteristics $(c_1^* < c_0^*,\ \rho_1^* < \rho_0^*)$ at parameters $c_0^* = 3000\ \frac{m}{s}$; $c_1^* = 2100\ \frac{m}{s}$; $\rho_0^* = 3000\ \frac{kg}{m^3}$; $\rho_1^* = 2700\ \frac{kg}{m^3}$; are summarized in Figs. 8-12 depending on length of the rod beginning section.

Table 1: Frequencies $f_1^*,\ f_2^*$at various sound speed and lengths $(c_1^*)$of the beginning rod section with changed acoustic properties.

	$c_1^* = 3000\ m/s$		$c_1^* = 2500\ m/s$		$c_1^* = 2100\ m/s$	
	$f_1^*,\ Hz$	$f_2^*,\ Hz$	$f_1^*,\ Hz$	$f_2^*,\ Hz$	$f_1^*,\ Hz$	$f_2^*,\ Hz$
$l^* = 2\ m$	375	1125	313	938	263	788
$l^* = 4\ m$	188	563	156	470	131	394
$l^* = 6\ m$	125	375	104	313	88	263
$l^* = 8\ m$	94	281	78	234	66	197
$l^* = 10\ m$	75	225	63	188	53	158

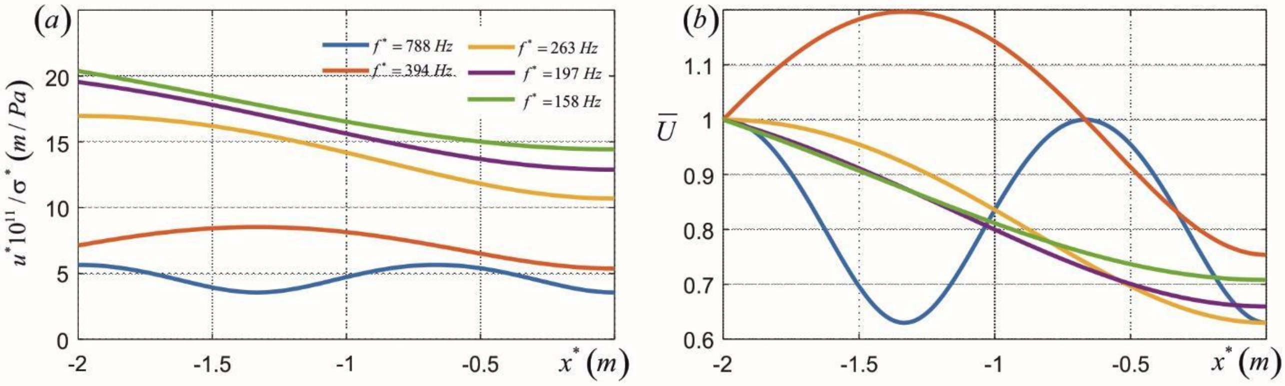

Fig. 8: Distribution of oscillation amplitudes within the beginning section of length *l=2*: (a) dimensional amplitudes, (b) amplitudes related to the amplitude at the loading point.

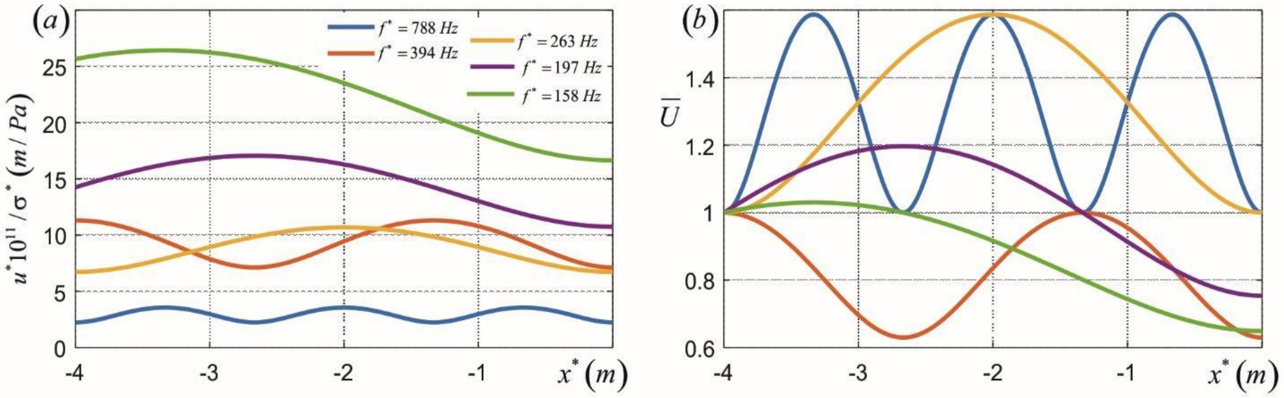

Fig. 9: Distribution of oscillation amplitudes within the rod beginning section of length *l=4*: (a) dimensional amplitudes, (b) amplitudes related to the amplitude at the loading point.

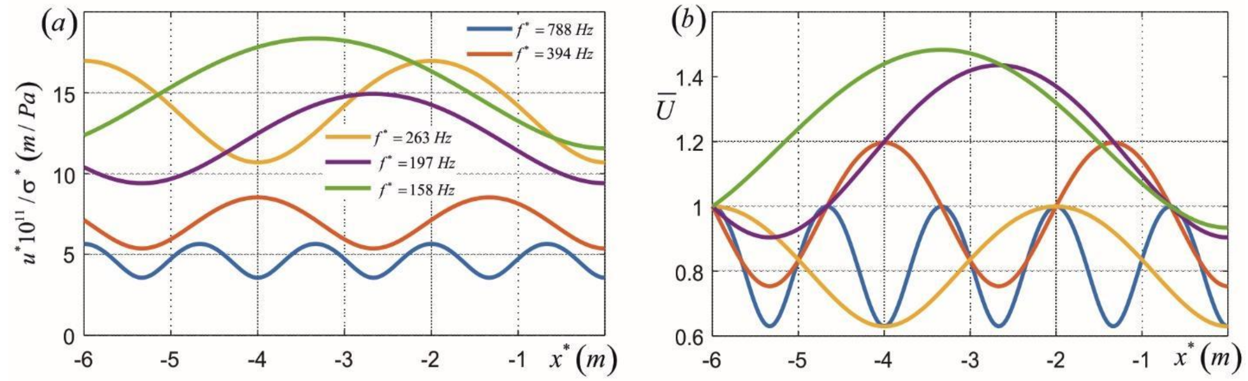

Fig. 10: Distribution of oscillation amplitudes within the rod beginning section of length *l=6*: (a) dimensional amplitudes, (b) amplitudes related to the amplitude at the loading point.

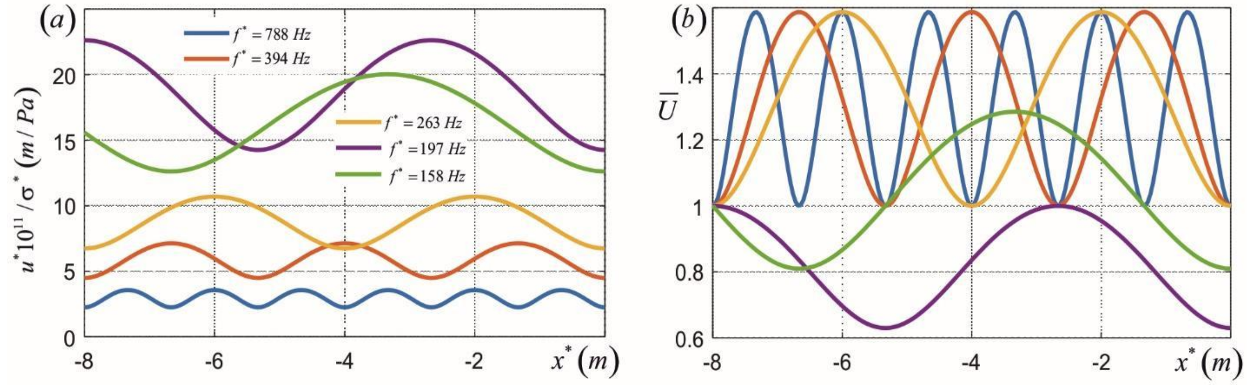

Fig. 11: Distribution of oscillation amplitudes within the rod beginning section of length *l=8*: (a) dimensional amplitudes, (b) amplitudes related to the amplitude at the loading point.

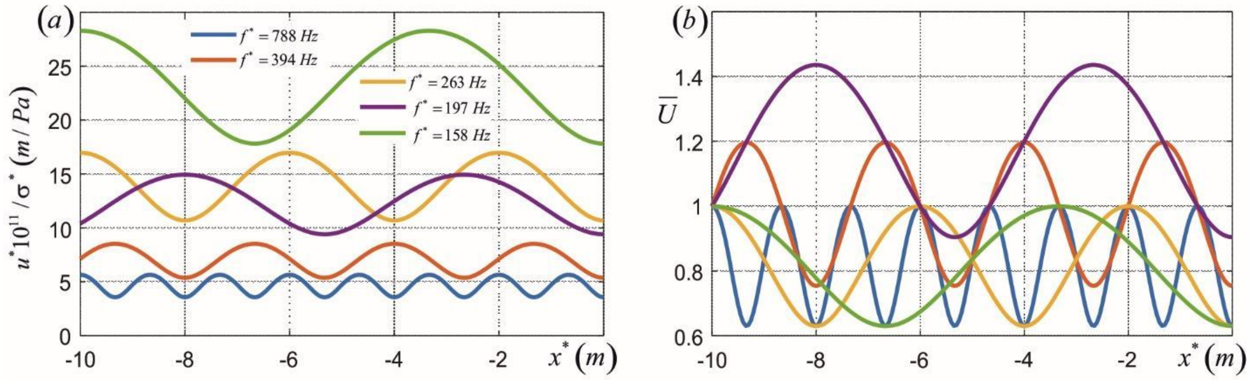

Fig. 12: Distribution of oscillation amplitudes within the rod beginning section of length *l=10*: (a) dimensional amplitudes, (b) amplitudes related to the amplitude at the loading point.

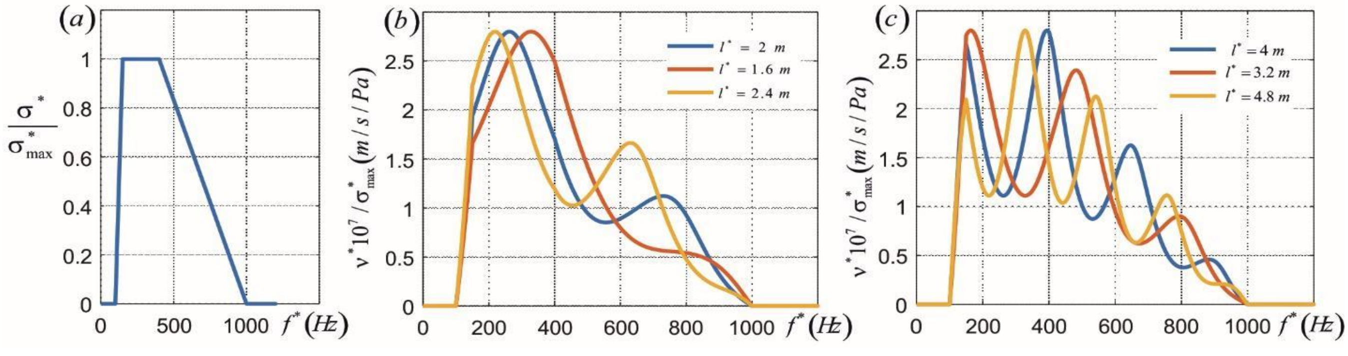

Fig. 13: Amplitude spectra of the load (a) and the velocity of displacements at the point of load application (b, c) and $c_0^* = 3000\ \frac{m}{s}$. $c_1^* = 2100\ \frac{m}{s}$. $\rho_0^* = 3000\ \frac{kg}{m^3}$. $\rho_1^* = 2700\ \frac{kg}{m^3}$.

The distribution of the oscillation amplitudes shows that with a decrease in the length of the rod beginning section, the number of extremes decreases and the extrema values shift to the diapason of higher frequencies. Fig. 13 illustrate this fact demonstrating the spectra of the displacement velocity obtained for different values of the length *l* and the same amplitude spectrum of the load.

According to the proposed analogy, it can be inferred that similar patterns in the distribution of oscillation amplitudes occur within the failure zone ahead of the excavation face. Under normal (stable) conditions of roadway advancement, the distance between the excavation face and the boundary of the undisturbed rock mass remains relatively constant. As a result, the averaged spectrum of recorded oscillations also remains stable and can be regarded as a baseline. Deviations from this baseline, such as the emergence of higher-frequency components, should be interpreted as indicators of approaching the boundary of the intact rocks to the excavation face. This finding can therefore be regarded as a rise in the probability of dynamic phenomena.

It should be noted, however, that the presented model of amplitude distribution in the near-face area does not account for the effects of boundary surfaces or wave attenuation, which would reduce oscillation amplitudes with increasing distance from the point of load application. Nevertheless, variations in the displacement velocity spectrum at the load application point are reasonably assumed to indicate changes in the dimensions of the failure zone ahead of the excavation face.

4. Conclusion

A one-dimensional (1-D) mathematical model of elastic wave propagation has been employed to analyze the features of harmonic oscillations ahead of the face of a horizontal underground roadway. These oscillations arise due to the interaction between a cutting tool and the surrounding rock, leading to localized rock failure. The nature of wave propagation in this scenario is primarily governed by the acoustic properties of the medium, which change due to the presence of a failure zone ahead of the excavation face. Given that the mechanical and acoustic properties of fractured rock differ significantly from those of intact rock mass, the model of wave propagation in a semi-infinite rod has been used to describe these processes.

In this model, the finite-length section of the rod, which possesses altered acoustic properties relative to the infinite part, is associated with the failure zone formed ahead of the excavation face. Despite certain idealizations inherent in this approach, the model successfully captures essential trends in wave behavior and demonstrates that the amplitude-frequency response of the oscillations ahead of the roadway face is closely linked to the quality of the surrounding rock mass. Specifically, this relationship is quantified through the Geological Strength Index (GSI), which influences the length l of the failure zone. The failure zone length is determined within the framework of an elastic-plastic constitutive model and the generalized Hoek-Brown criterion, both of which account for the mechanical response of fractured rock under stress.

The analysis of wave propagation in the semi-infinite rod model reveals that both displacement amplitudes and displacement velocity amplitudes are significantly affected by the length l of the rod finite section. A key finding is that as the length l decreases, the number of amplitude extrema in the wave distribution decreases correspondingly, and these extrema shift toward higher frequencies. This means that the reduction of the failure zone ahead of the roadway face will also cause the occurrence of extreme vibration amplitudes at higher frequencies. Consequently, the appearance of high frequencies in the amplitude-frequency spectrum signals a reduction in the zone of inelastic deformations ahead of the roadway face, *i.e.*, a reduction in the distance between the face and the undisturbed part of the rock mass, where elastic energy accumulates. This result suggests that the frequency characteristics of the oscillations can serve as a diagnostic indicator of changes in the failure zone and, by extension, the mechanical state of the rock mass near the excavation front.

In practical underground excavation scenarios, it is feasible to define an oscillation spectrum that characterizes a stable state of rocks, free from indications of impending dynamic instability. This reference spectrum can be used as a baseline for monitoring the stability of the excavation process. Deviations from this baseline, particularly the emergence of higher-frequency components in the recorded signals, can serve as an early warning of changes in rock mass behavior. Specifically, the appearance of high-frequency oscillations indicates that the boundary between fractured and intact rock mass is approaching the excavation face, increasing the likelihood of dynamic events such as rock bursts or sudden failure.

Therefore, the findings of this study provide a foundation for the development of predictive techniques for assessing dynamic failure hazards in underground excavations. By analyzing the amplitude-frequency characteristics of recorded signals, it is possible to detect early signs of rock instability, thereby enabling proactive safety measures. The technical implementation of this monitoring approach, along with its practical applicability, is further discussed in the papers.[46,47]

Acknowledgments

The research is funded by the Ministry of Science and Education of the Republic of Kazakhstan, project No.

AP19680130

Conflict of Interest

There is no conflict of interest.

Supporting Information

Not applicable.

References

[1] S. B. Chai, J. C. Li, Q. B. Zhang, H. B. Li, N. N. Li, Stress wave propagation across a rock mass with two non-parallel joints, *Rock Mechanics and Rock Engineering*, 2016, **49**, 4023-4032, doi: 10.1007/s00603-016-1068-z.

[2] A. M. Meirmanov, M. Nurtas, Mathematical models of seismic in composite media: elastic and poroelastic components, *Electronic Journal of Differential Equations*, 2016, **184**, 1-22.

[3] A. M. Meirmanov, S. Mukhambethzanov, M. Nurtas, Seismic in composite media: elastic and poroelastic components, *Siberian Electronic Mathematical Reports*, 2016, **13**, 75-88.

[4] Z. Yang, M. Ge, S. Wang, Characteristics of transmitting channel wave in a coal seam, *Mining Science and Technology (China)*, 2009, **19**, 331-336, doi: 10.1016/S1674-5264(09)60062-4.

[5] H. Zhao, B. Chen, C. Zhu, Decision tree model for rockburst prediction based on microseismic monitoring, *Advances in Civil Engineering*, 2021, **2021**, 8818052, doi: 10.1155/2021/8818052.

[6] R. Shen, L. Qiu, E. Zhao, X. Han, H. Li, Z. Hou, X. Zhang, Experimental study on frequency and amplitude characteristics of acoustic emission during the fracturing process of coal under the action of water, *Safety Science*, 2019, **117**, 320-329, doi: 10.1016/j.ssci.2019.04.031.

[7] L. Qiu, D. Song, Z. Li, B. Liu, J. Liu, Research on AE and EMR response law of the driving face passing through the fault, *Safety Science*, 2019, **117**, 184-193, doi: 10.1016/j.ssci.2019.04.021.

[8] E. Zhao, E. Wang, H. Chen, Study on dynamic parameters and energy dissipation characteristics of coal samples under dynamic load and temperature, *Processes*, 2023, **11**, 3326, doi: 10.3390/pr11123326.

[9] Accidents in Kazakhstani mines: their tragic count, November 3, 2022.

[10] M. S. Khaidarov. Geodynamics of gas-dynamic phenomena on the example of central Asia, NNC RK Bulletin, 3, 2020.

[11] N. Koroleva. Six killed in mine explosion in Kazakhstan, November 7, 2021.

[12] E. Weber. Another Deadly Mine Accident, Astana Reclaims “Arcelor” Assets? October 28, 2023.

[13] Kazakhmys mine collapse: bodies of seven miners brought to surface, February 18, 2025.

[14] O.Sdvyzhkova, Y.Golovko, , D.Klymenko, Effect of harmonic oscillations on a crack initiation in the rock mass, *Naukovyi Visnyk Natsionalnoho Hirnychoho Universytetu*, 2017, **4**, 13-18.

[15] M. Nurtas, Z. Baishemirov, Y. Aizhan, A. Aizhan, 2-D Finite Element method using “eScript” for acoustic wave propagation *Proceedings of the 6th International Conference on Engineering & MIS*, Series, 2020, 1-7, doi: 10.1145/3410352.3410774.

[16] M. Nurtas, Z. Baishemirov, V. Tsay, M. Tastanov, Z. Zhanabekov, Convolutional neural networks as a method to solve estimation problem of acoustic wave propagation in poroelastic media, *News of the National Academy of Sciences of the Republic of Kazakhstan*, 2020, **4**, 52-60, doi: 10.32014/2020.2518-1726.65.

[17] J. Santamarina, G. Cascante, Stress anisotropy and wave propagation: A micromechanical view, *Canadian Geotechnical Journal*, 1996, **33**, 770-782, doi: 10.1139/t96-102-323.

[18] R. Sebastian, T. G. Sitharam, Long-wavelength propagation of waves in jointed rocks - study using resonant column experiments and model material, *Geomechanics and Geoengineering,* 2016, **11**, 281-296, doi: 10.1080/17486025.2016.1139753

[19] A. Biryukov, N. Tisato, G. Grasselli, Attenuation of elastic waves in bentonite and monitoring of radioactive waste repositories, *Geophysical Journal International*, 2016, **205**, 105-121, doi: 10.1093/gji/ggv548.

[20] D. Chen, X. Liu, W. He, C. Xia, F. Gong, X. Li, X. Cao, Effect of attenuation on amplitude distribution and b value in rock acoustic emission tests, *Geophysical Journal International*, 2021, **229**, 933-947.

[21] F. Bouchaala, M. Y. Ali, J. Matsushima, Attenuation study of a clay-rich dense zone in fractured carbonate reservoirs, *Geophysics*, 2019, **84**, B205-B216, doi: 10.1190/geo2018-0419.1.

[22] G. Zhang, X. Li, S. Zhang, T. Kundu, Investigation of frequency-dependent attenuation coefficients for multiple solids using a reliable pulse-echo ultrasonic measurement technique, *Measurement*, 2021, **177**, 109270, doi: 10.1016/j.measurement.2021.109270.

[23] B.-C. Kim, J. Chen, J.-Y. Kim, Relation between crack density and acoustic nonlinearity in thermally damaged sandstone, *International Journal of Rock Mechanics and Mining Sciences*, 2020, **125**, 104171, doi: 10.1016/j.ijrmms.2019.104171.

[24] X. Liu, F. Xiong, Q. Xie, X. Yang, D. Chen, S. Wang, Research on the attenuation characteristics of high-frequency elastic waves in rock-like material, *Materials*, 2022, **15**, 6604, doi: 10.3390/ma15196604.

[25] W. Zhao, C. Qin, W. Chen, X. Tan, Elastic wave propagation through a layered rock mass with adhesive bedding planes, *International Journal of Geomechanics*, 2023, **23**, 04023222, doi: 10.1061/ijgnai.gmeng-8453.

[26] Q. Yang, L. Fan, X. Du, Experimental investigation on the frequency-spectrum characteristic of stress wave propagation through thermally treated granite, *International Journal of Rock Mechanics and Mining Sciences*, 2023, **170**, 105527, doi: 10.1016/j.ijrmms.2023.105527.

[27] D. Hua, Q. Jiang, A general equivalent continuum model and elastic wave velocity analysis of jointed rock masses, *International Journal of Rock Mechanics and Mining Sciences*, 2023, **170**, 105500, doi: 10.1016/j.ijrmms.2023.105500.

[28] Z. Zhang, J. Zhu, J. Deng, A comparative study for determining rock joint normal stiffness with destructive uniaxial compression and nondestructive ultrasonic wave testing, *Journal of Rock Mechanics and Geotechnical Engineering*, 2023, **15**, 1700-1712, doi: 10.1016/j.jrmge.2022.10.010.

[29] X. Zhang, M. Xie, Z. Huang, Y. Du, L. Zhang, Z. Wu, Z. Fan, Experimental study on the vibration characteristics of dangerous rock mass under constant micromotion, *Advances in Civil Engineering*, 2023, **2023**, 6323929, doi: 10.1155/2023/6323929.

[30] H. Yang, Q. Zhao, D. Han, Q. Lei, H. Wu, X. Huang, Z. Chen, Y. Huang, Elastic wave propagation and attenuation across cemented rock fractures under tension, *International Journal of Rock Mechanics and Mining Sciences*, 2025, **186**, 106024, doi: 10.1016/j.ijrmms.2025.106024.

[31] X. Fang, A one-dimensional stress wave model for analytical design and optimization of oscillation-free force measurement in high-speed tensile test specimens, *International Journal of Impact Engineering*, 2021, **149**, 103770, doi: 10.1016/j.ijimpeng.2020.103770.

[32] Z. Xu, P. Lognonné, A comprehensive theory for 1-D (an)elastic medium deformation due to plane-wave fluid pressure perturbation, *Geophysical Journal International*, 2024, **236**, 1499-1512, doi: 10.1093/gji/ggae005.

[33] A. Andrukhiv, M. Sokil, B. Sokil, S. Fedushko, Y. Syerov, V. Karovic Jr, T. Klynina, Influence of impulse disturbances on oscillations of nonlinearly elastic bodies, *Mathematics*, 2021, **9**, 819, doi: 10.3390/math9080819.

[34] A. Gomez, G. Rus, N. Saffari, Wave propagation in a fractional viscoelastic tissue model: application to transluminal procedures, *Sensors*, 2021, **21**, 2778, doi: 10.3390/s21082778.

[35] Y. Chen, E. Liu, P. He, A binary-medium-based constitutive model for geological materials based on the statistical meso-breakage concept and mean-field homogenization, *European Journal of Environmental and Civil Engineering*, 2023, **27**, 3425-3448, doi: 10.1080/19648189.2022.2136763.

[36] C. Zhang, Z. Zhu, S. Wang, X. Ren, C. Shi, Stress wave propagation and incompatible deformation mechanisms in rock discontinuity interfaces in deep-buried tunnels, *Deep Underground Science and Engineering*, 2022, **1**, 25-39, doi: 10.1002/dug2.12016.

[37] Z. Cui, Q. Sheng, X. Leng, Analysis of S wave propagation through a nonlinear joint with the continuously yielding model, *Rock Mechanics and Rock Engineering*, 2017, **50**, 113-123, doi: 10.1007/s00603-016-1108-8.

[38] H. Li, N. Zhou, J. Huang, M. Zhao, W. Liao, X. Zhao, X. Du, Analytical solution of longitudinal seismic response of circular tunnel across soil-rock stratum based on improved elastic foundation beam model, *Computers and Geotechnics*, 2023, **159**, 105383, doi: 10.1016/j.compgeo.2023.105383.

[39] X. Gao, C. Liu, H. Zhang, K. Yang, Y. Hu, X. Guo, The change in the shape characteristics of the plastic zone in the surrounding rock of an auxiliary retracement channel and a reasonable channel spacing determination method, *Applied Sciences*, 2023, **13**, 10543, doi: 10.3390/app131810543.

[40] G. Guo, H. Li, Finite–discrete element method prediction of advanced fractures in extra-thick coal seams based on a constitutive model of rock deformation–fragmentation failure process, *Processes*, 2023, **11**, 675, doi: 10.3390/pr11030675.

[41] X. Sun, W. Zhao, J. Wang, M. Jiang, F. Shen, Y. Zhang, C. Miao, Research on failure mechanism and stability control technology of dynamic pressure roadway in ultra-thick coal seams under a high depth of cover, *Mining, Metallurgy & Exploration*, 2023, **40**, 1955-1972, doi: 10.1007/s42461-023-00846-7.

[42] R. Shan, Y. Wei, C. Wang, Z. Li, Y. Li, D. Liu, X. Zhao, Research on the failure mechanism of surrounding rock in a dynamic pressure roadway and active and passive coordinated support technology, *Applied Sciences*, 2024, **14**, 1858, doi: 10.3390/app14051858.

[43] E. Hoek, E. T. Brown,The Hoek–Brown failure criterion and GSI – 2018 edition, Journal of Rock Mechanics and Geotechnical Engineering, 2019, **11**, 445-463, doi: 10.1016/j.jrmge.2018.08.001.

[44] M. Nurtas, F. Tokmukhamedova, A. Ydyrys, Z. Zhantaev, S. Nurakynov, B. Iskakov, A. Altaibek, B. Matkerim, Application of finite element method for solving seismoacoustic modeling problems in poroelastic composite media, *Engineered Science*, 2023, **26**, 1030, doi: 10.30919/es1030.

[45] E. Hoek, E. T. Brown, Practical estimates of rock mass strength, *International Journal of Rock Mechanics and Mining Sciences*, 1997, **34**, 1165-1186, doi: 10.1016/S1365-1609(97)80069-X.

[46] O. Sdvyzhkova, Y. Golovko, N. M. University, M. Dubytska, N. M. University, D. Klimenko, N. M. University, Studying a crack initiation in terms of elastic oscillations in stress strain rock mass, *Mining of Mineral Deposits*, 2016, **10**, 72-77, doi: 10.15407/mining10.02.072.

[47] O. Shashenko, Y. Golovko, D. Klymenko, Rigidity effect of

the mine geophone mounting on its frequency response, *Naukovyi Visnyk Natsionalnoho Hirnychoho Universytetu*, 2021, 44-50, doi: 10.33271/nvngu/2021-3/044.

Open Access